Deep neural network based unsteady flamelet progress variable approach in a supersonic combustor

Sinan Demir*, Prithwish Kundu†, Cody Nunno*, Sibendu Som‡
Argonne National Laboratory, Lemont, IL, 60439, USA

Robert Baurle§ and Tomasz Drozda§
NASA Langley Research Center, Hampton, VA, 23681, USA

Higher dimensional flamelet manifolds are essential in capturing the coupled effects of pressure gradients and unsteady chemical kinetics observed in supersonic combustion applications. Previous studies have validated the feasibility of using deep neural networks as an alternative to computationally intensive multidimensional flamelet table storage and lookup. This approach has demonstrated a significant reduction in memory footprint and enabled the use of larger dimensional tabulated manifolds for supersonic combustion in canonical problems. In this study, the Unsteady Flamelet Progress Variable (UFPV)-ANN model implemented in the VULCAN-CFD code is validated by the Burrows-Kurkov supersonic mixing/combustion configuration. The well characterized experimental problem consists of hydrogen injection into a supersonic vitiated crossflow that results in a lifted flame structure. The initial model consists of a 4-dimensional table where the independent variables $\tilde{Z}$, $\tilde{C}$, $\tilde{X_{st}}$, $\tilde{P}$ are tabulated using an unsteady flamelet code with boundary conditions corresponding to the vitiated air conditions. The results show the development of a lifted flame structure and overall acceptable agreement with finite-rate chemistry (FRC) simulation and the experimental data. Moreover, direct mapping between the independent variables and the flamelet table is replaced by a deep neural network for significant memory reduction. The results indicate that the UFPV-ANN approach can retrieve the same solution as the memory intensive lookup table approach.

I. Nomenclature

χ_{st}	=	Stoichiometric scalar dissipation rate
Z	=	Mixture fraction
$Z^{"2}$	=	Mixture fraction variance
C	=	Progress variable
Y	=	Species mass fraction
T	=	Temperature
P	=	Pressure
ρ	=	Density
C_p	=	Specific heat at constant pressure
Sc	=	Schmidt number
Pr	=	Prandtl number

*Postdoctoral Appointee, Multi-Physics Computation, 9700 S. Cass Avenue, AIAA Member
†Research Scientist, Multi-Physics Computation, 9700 S. Cass Avenue, AIAA Member
‡Section Manager, Multi-Physics Computation, 9700 S. Cass Avenue, AIAA Member
§Aerospace Research Scientist, Hypersonic Airbreathing Propulsion Branch, MS 168, AIAA Associate Fellow

II. Introduction

The scramjet is a promising air-breathing propulsion technology that offers potential to enable efficient, reusable, and safe high-speed flights. CFD has the potential to be a powerful tool for the designing and optimization of these engines, but computational modeling brings some challenges. Physical flow processes in a scramjet combustor are highly nonlinear and coupled with shock/rarefaction waves, turbulent mixing, boundary layer interactions and chemical kinetics. Moreover, highly compressible effects in the flow field need to be captured by numerical algorithms with minimal dissipation in order to be capable of representing the shock-turbulence and combustion interactions. Turbulence closure models should therefore be capable of representing the key features of turbulent mixing-chemistry interactions at all unresolved scales. Furthermore, detailed chemical kinetics are required to capture the main combustion processes. As a result, the development of turbulence models capable of capturing all the important turbulent-combustion interactions at different flow conditions in a scramjet combustor remains as an incomplete task, which commands both the fundamental interests and practical relevance.

A number of modeling approaches[1] like FRC, PaSR, LEM, TPDF have been developed over the years. Briefly, FRC, also known as a no-model approach, neglects turbulent-chemistry interaction (TCI). The PaSR model is based on the assumption of adiabatic microstructures where all the chemical reactions occur only in these localized regions. PaSR is based on algebric relations including model constants which may need to be tuned at different combustion regimes. TPDF and LEM methods overcome this issue and are agnostic of the combustion regime. However, both TPDF and LEM are computationally intensive. In the flamelet approach, chemistry is parameterized as a function of a few tracking parameters and stored in tabulated look-up tables, which allows use of detailed and complex chemical mechanisms. During the CFD simulations, thermochemical quantities are interpolated from the look-up tables. However, the low-dimensionality of the flamelet model may under certain flow conditions lead to poor accuracy. This becomes more pronounced in supersonic combustion where higher dimensional flamelet manifolds are required to accurately predict fundamental physics.[2] For example, pressure should be added as an additional variable within the flamelet tables to adequately predict the effect of compression/expansion waves.[2,3] However, an increase in the dimension of the flamelet table in a classical way requires high dimensional interpolation of parameterized variables within the flamelet tables and causes immense memory allocation. It should be noted that computational requirements increase nonlinearly as the dimensionality of the table increases. In summary, adding dimensions to the flamelet model increases the memory footprint and retrieval costs, which in turn makes the flamelet models less competitive with the detailed kinetics they are trying to efficiently replace.

Previous studies have demonstrated the implementation of the UFPV-ANN approach for a canonical problem in the VULCAN CFD code.[4] In this study, we extend the testing and validation towards more realistic cases, i.e., the Burrows-Kurkov[5,6] supersonic combustor. The flamelet tables are generated using an in-house flamelet code.[7] The current implementation can efficiently accommodate up to 5D tables along with a linear multi-dimensional lookup scheme. This work focuses on predictions of a deep neural network based framework that can replace multidimensional tables for reacting flow calculations.

The paper is organized as follows. Section III describes the original Burrows and Kurkov experimental configuration, and provides details of the computational setup. Section IV provides the model formulations for the UFPV approach and the basic details of the UFPV-ANN framework. In the results section, the accuracy of the UFPV and UFPV-ANN models is examined with respect to both experimental data and FRC simulation. The results section concludes with a subsection discussing some challenges faced in this study regarding the solution of non-normalized versus normalized transport equation for the progress variable.

III. Problem Definition and Computational Setup

A. Burrows and Kurkov Experimental Configuration

The Burrows-Kurkov[5,6] supersonic mixing/combustion configuration has been widely utilized in the literature for the validation of the combustion models in the context of RANS and LES studies.[8–10] It provides comprehensive experimental data for stagnation temperature, pitot and wall pressures, species mole fractions, and on-set ignition location measurements, for both inert gas mixing (where nitrogen is replaced with oxygen in the air stream) and vitiated-air mixing/reacting gas flow conditions at different locations of the combustor. A schematic of the original Burrows and Kurkov experimental configuration is shown in Fig. 1. In this configuration, hydrogen from a slot is injected into the test section at Ma 1.0 and 314 K conditions. The vitiated air at Mach 2.5 and 1250K enters the test

section where it mixes with the hydrogen and combustion occurs downstream. In the case of inert gas mixing, the static temperature is about 1150K.

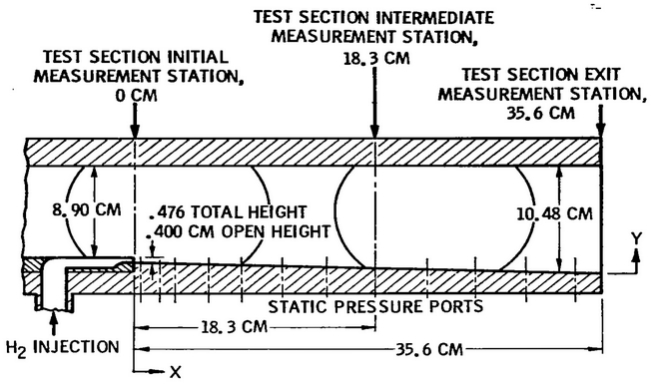

Figure 1. Schematic of the Burrows and Kurkov supersonic combustor (taken from Ref.[5])

B. Computational Setup Details

The computational platform utilizes a compressible multi-block flow solver called VULCAN-CFD. The VULCAN-CFD code is a finite volume solver that provides a comprehensive set of numerical tools that enable the modeling of reacting flows from subsonic to hypersonic speeds. The solver is fully parallelized using MPI. It can accommodate structured as well as unstructured grids with RANS, LES or hybrid RANS-LES formulations.

The individual species viscosities and thermal conductivities are computed from the polynomial curve fits of McBride.[11] The computed coefficients are then combined to obtain mixture-averaged values with the use of empirical relations. The moleculer diffusion coefficient is assumed constant for all the species and obtained by specifying a Schmidt number of 0.5. The turbulent simulations are performed in the context of RANS, which uses Menter's $k-\omega$ turbulence model[12] with a turbulent Schmidt number of 0.5, which is widely used for a broad range of flows and appears to be a reasonable closure model, especially in the attached boundary layer regions.

The computational setup consists of a 2D spatial domain and a view of the computational grid used in the CFD simulations is shown in Fig. 2. In addition to the original Burrows-Kurkov experimental test configuration given in,[5] a converging-diverging nozzle was designed to replicate the Mach 2.5 coreflow to better approximate the facility boundary layer development. A finer mesh near the wall region is used to capture the gradients for proper prediction of the boundary layer development given the use of wall functions in this effort. This provides an average $y+$ of 7 for the wall adjacent cells. No-slip, isothermal compressible wall condition at a constant temperature of 350K is specified at the walls. Supersonic outflow boundary condition with 1^{st} order extrapolation of all the variables is applied at the cell center of the ghost cells. The nominal test section inflow conditions considered in the CFD simulations are given in table 1.

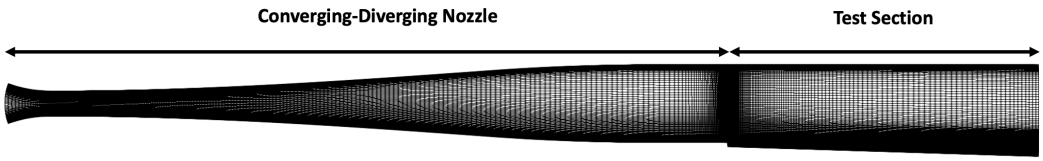

Figure 2. Computational domain and view of computational grid used in the CFD simulations

In the current simulation procedure, we use a multiregion simulation strategy in which the nozzle and test-section are solved separately using an elliptic solver. Time integration is performed by an explicit two-stage Runge-Kutta scheme and the time-step is determined from a CFL condition (CFL$<$1) for numerical stability. At each computational cell, the local time-step Δt is determined based on the CFL number. As a result, the time-step Δt in the combustor section spatially varies between $10^{-12} - 10^{-6}$ secs.

Table 1. Burrows-Kurkov reference inflow conditions

	$U[m/s]$	$T[K]$	$P[Pa]$	Y_{H_2O}	Y_{O_2}	Y_{N2}	Y_{H_2}
Pure mixing case:							
Inert gas	1695	1082	94,595	0.2162	0.0509	0.7324	0.0005
Hydrogen	1304	258	110,000	0.0	0.0	0.0	1.0
Combustion case:							
Vitiated air	1775.2	1233	97,081	0.256	0.258	0.486	0.0
Hydrogen	1295	257	108,257	0.0	0.0	0.0	1.0

IV. Model Formulations

A. Unsteady Flamelet-Progress Variable (UFPV) Approach

This section briefly describes the transport equations, which are used to construct the flamelet table for use with VULCAN-CFD. We use the compressible UFPV approach[13] in a RANS formulation. The flamelet equations are obtained by applying a Crocco-type transformation to the species and energy transport equations to recast them from spatial coordinates into a 1D mixture fraction space.[14] The equations in unsteady form are shown below:

$$\rho\frac{\partial Y_i}{\partial t} = \rho\frac{\chi}{2}\frac{\partial^2 Y_i}{\partial Z^2} + \dot{\omega}_i \tag{1}$$

$$\rho\frac{\partial T}{\partial t} - \rho\frac{\chi}{2}\frac{\partial^2 T}{\partial Z^2} = \frac{1}{C_p}\left(\frac{\partial P}{\partial t} - \sum \dot{\omega}_i h_i\right) \tag{2}$$

In the flamelet approach, the CFD solver solves for the mixture fraction transport equation which is then used to look-up the local thermochemical state encoded in the flamelet table using the equations shown above. In addition to the mixture fraction, the flamelet table is parameterized by different stoichiometric scalar dissipation rates through a χ_{st} dimension and can also include unsteadiness via the progress variable, C. The flamelet table can be further extended to account for the TCI effects by convolution of the solutions with a presumed PDF, for example. In the UFPV formulation implemented in VULCAN-CFD, the table is parameterized using 5 independent variables $Y = f(P, C, \chi_{st}, Z''^2, Z)$.

In the current work, the flamelet equations were solved using an in-house code[7] using an analytical Jacobian and a sparse solver. The resulting flamelet table stores the species mass fractions and progress variable source terms for a range of the independent variables. The flamelet table used in the UFPV simulations in this study has 5x16x151x2x101 points, and Z, C and χ_{st} are non-uniformly distributed. In addition to the existing continuity, momentum and total energy equations, transport equations for Favre averaged mixture fraction, $\bar{\rho}\tilde{Z}$, mixture fraction variance, $\bar{\rho}\widetilde{Z''^2}$ and progress variable, $\bar{\rho}\tilde{C}$ were implemented into VULCAN-CFD solver. The source term for the progress variable equation is retrieved from the flamelet table.

$$\frac{\partial(\bar{\rho}\widetilde{Z})}{\partial t} + \frac{\partial(\bar{\rho}\widetilde{u_i}\widetilde{Z})}{\partial x_i} = \frac{\partial}{\partial x_i}\left[\left(\frac{\mu}{Sc} + \frac{\mu_t}{Sc_t}\right)\frac{\partial\tilde{Z}}{\partial x_i}\right] \tag{3}$$

$$\frac{\partial(\bar{\rho}\widetilde{u_i}\widetilde{Z''^2})}{\partial x_i} = \frac{\partial}{\partial x_i}\left[\left(\frac{\mu}{Sc} + \frac{\mu_t}{Sc_t}\right)\frac{\partial\widetilde{Z''^2}}{\partial x_i}\right] + 2\frac{\mu_t}{Sc_t}\left(\frac{\partial\widetilde{Z}}{\partial x_i}\right)^2 - \bar{\rho}\widetilde{\chi} \tag{4}$$

$$\frac{\partial(\bar{\rho}\widetilde{C})}{\partial t} + \frac{\partial(\bar{\rho}\widetilde{u_i}\widetilde{C})}{\partial x_i} = \frac{\partial}{\partial x_i}\left[\left(\frac{\mu}{Sc} + \frac{\mu_t}{Sc_t}\right)\frac{\partial\widetilde{C}}{\partial x_i}\right] + \overline{\dot{\omega}_c} \tag{5}$$

The mean scalar dissipation rate, $\tilde{\chi}$, appears in the last term of Eq. (4) and is modeled as $\widetilde{\chi} = C_x\tilde{\varepsilon}/\tilde{k}\widetilde{Z''^2}$ with $C_x = 2.0$. In this study, the progress variable is defined as the mass fraction of H_2O, $Y_C = Y_{H_2O}$. Then the normalized progress variable, C, is calculated by

$$C = \frac{Y_C - Y_{C,min}(Z, \chi_{st}, P)}{Y_{C,max}(Z, \chi_{st}, P) - Y_{C,min}(Z, \chi_{st}, P)} \tag{6}$$

More details on the normalization procedure of the progress variable as well as differences between normalized and non-normalized solution of the transport equation for the progress variable will be presented in the results section.

In addition to the above transport equations, a framework to access up to a 5D flamelet table through a linear, multidimensional interpolation approach was implemented into VULCAN-CFD. At each time-step, the species mass fractions and progress variable source term are retrieved from the table. The temperature is then calculated from the transported total energy and the mass fractions retrieved from the table.

B. UFPV-ANN approach

In order to overcome the issues of high memory footprint and retrieval costs associated with large flamelet tables, researchers have developed novel strategies using artificial neural networks (ANNs).[4,15] ANNs are inspired by biological neural networks, which consist of an interconnected network of artificial neurons relating one or more outputs to a set of inputs. A schematic of a multi-layer neural network is shown in Fig. 3, and it consists of three parts: (i) $input\ layer$ where the list of input variables, five in this case, are accommodated; (ii) $hidden\ layers$ that use transfer functions to weight and propagate the input variables to the output layer; (iii) $output\ layer$ that contains all the trained vector data, in this case species mass fractions and progress variable reaction term. The ANN training process is generally started by a random initialization of weights and biases. As the training process advances, weights and biases are adjusted to optimize the ANN predictions to reduce the error. Gradient-based and second-order methods are the two commonly used error minimization algorithms. Similar to,[15] we use a second-order Levenberg–Marquardt (LM) algorithm.

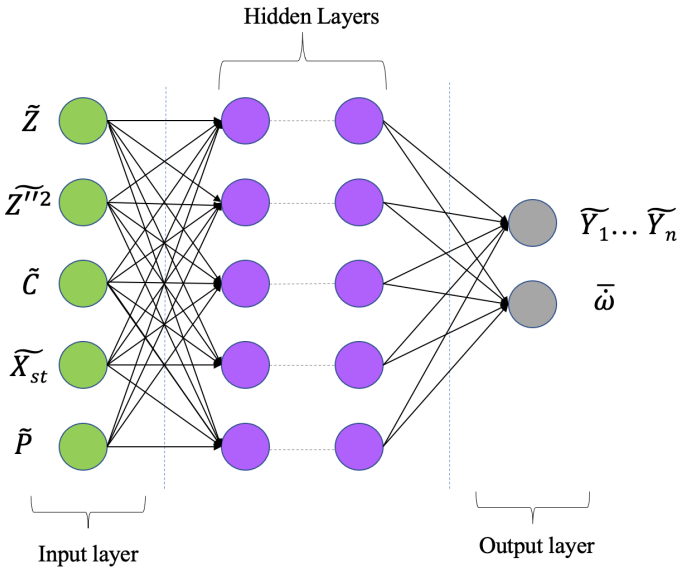

Figure 3. Schematic of deep neural network for 5D UFPV-ANN approach

In this study, a 7-step/7-species hydrogen-air chemical mechanism is used to build a 5D table for the combustion case. Next, the generated flamelet table is used to train ANNs using MATLAB - Deep Learning Toolbox. The independent variables are fed as inputs to the network and the species mass fractions are the outputs. All the species mass fractions in the table are first normalized between -1 and 1 and then used for training. The progress variable source terms are relatively more difficult to train. This is due to the fact that these values can change over many orders of magnitude in the reaction process. A small error in the network can still result in a large magnitude error during the inference stage. To partially address this issue, the progress variable source terms are first converted to a logarithmic scale before normalization and training. However, the accuracy of the UFPV-ANN simulations can still deteriorate, and the simulations can exhibit inaccurate results. To overcome this issue, the source terms can be retrieved from the flamelet table by interpolation, while the species mass fractions are obtained through the UFPV-ANN framework. Based on sensitivity studies in the previous work, 4 hidden layers with 9 neurons were used for this study. Eighty percent of the dataset is used for training and the rest is used for validation. The approach has also been

extensively validated in a previous study for subsonic applications.[15] A separate inference module was developed and implemented into the VULCAN-CFD code. This module can be used to read and retrieve data from ANNs using a *tanh* activation function, thereby replacing the memory intensive process of storing and probing large tables. This module is extendable to any type of flamelet model.

V. Results

In this section, we present computational results of inert-gas mixing and vitiated-air mixing/combustion cases with UFPV and UFPV-ANN approaches. Accuracy is examined based on the Burrows-Kurkov experimental data and the FRC simulation.

A. Inert-gas mixing

The Burrows-Kurkov experiments provide measurements for the stagnation temperature and pitot pressure at the combustor entrance ($x = 0.0$) and exit ($x = 35.59$ cm) locations respectively for the inert-mixing. These profiles along with the computational results are shown in Fig. 4. In both profiles, all computational results coincide with each other and show a good agreement with the experimental measurements. The thermal boundary layer analysis in these simulations indicated that the current nozzle design yields an inflow at the combustor entrance location near the lower wall, where the boundary layer is slightly thicker than the one indicated in the experiment (~ 1 cm). Moreover, there is some evidence of imperfect mixing in the vitiator that was not modeled in these simulations (as evidenced by the kink in the total temperature profile near $y = 4$ cm at the combustor entrance). This can explain the minor differences observed in the simulations. Comparison of mole fraction profiles for hydrogen, nitrogen and water at the combustor exit is given in Fig. 5, which indicates very good agreement with the experiments. This result shows the current turbulent closure model and turbulent Schmidt ($= 0.5$) and Prandtl number ($= 0.9$) values are able to capture the turbulent diffusion process quite well.

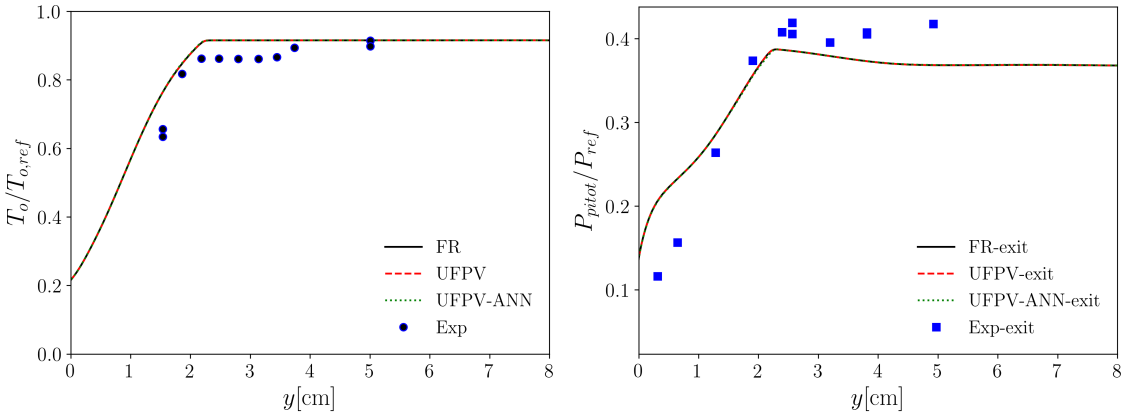

Figure 4. Stagnation temperature and pitot pressure profiles for inert-gas mixing: combustor entrance (left), combustor exit (right)

B. Vitiated air mixing/combustion

The UFPV model is tested here with four independent variables where $\tilde{Y}_i = \tilde{Y}_i(\tilde{Z}, \tilde{C}, \tilde{X}_{st}, \tilde{P})$. We omitted TCI to reduce the complexity of the problem for the presented results in this study, hence the variable $\widetilde{Z''^2}$ is tabulated with two points only (as a legacy of the flamelet solver) but set to 0.0 before the interpolations. This is in accord with the FRC simulations which omits the TCI as well.

The temperature and OH mass fraction contour plots at the test section are shown in Fig. 6 for FRC and UFPV calculations. Both results predict a lifted flame in the downstream region, however, flame stabilization location differs significantly. While the flame is stabilized at 18 cm for the FRC, this location is about 4 cm for the UFPV. Ignition on-set location and the flame front position can be clearly indicated with the OH mass fraction contours for the

simulations. In the literature, a wide range of flame lift-off heights (5-30 cm) were reported depending on the used combustion model, chemical mechanism, grid spacing, etc. The flame lift-off height for the FRC result is consistent with most of the studies, and within the range of 11-27 cm, which was reported in the Burrows-Kurkov experiments. To understand the difference in the flame lift-off height prediction obtained from the UFPV simulation, we repeated the UFPV simulation with $\tilde{X}_{st}$ fixed at its lowest value ($\tilde{X}_{st}$=1.0). Figure 7 indicates that this UFPV simulation yields a comparable flame lift-off height to the FRC and the experiment. In this exercise, the maximum temperature ($\sim 2700K$) is higher, however, this is consistent with the equilibrium temperature obtained from the unsteady flamelet solutions when $\tilde{X}_{st} = 1.0$. One possible explanation for this is that the scalar dissipation rate acts like an increased diffusion coefficient, thereby enhancing the diffusive transport in the mixture fraction space. However, this should be investigated in more detail, thereby we leave it for a future study.

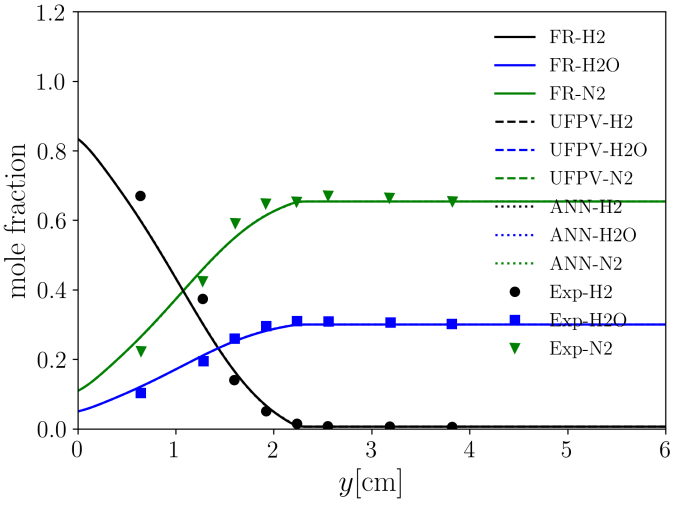

Figure 5. Mole fraction profiles at the combustor exit for inert-gas mixing

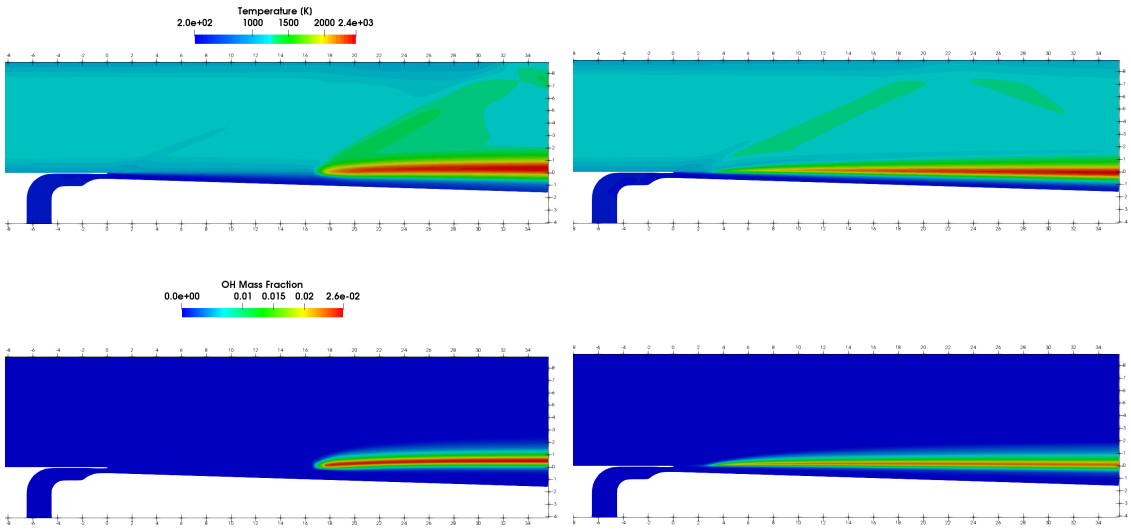

Figure 6. Contours of the temperature and $\tilde{Y}_{OH}$ obtained using FRC (left) and UFPV (right).

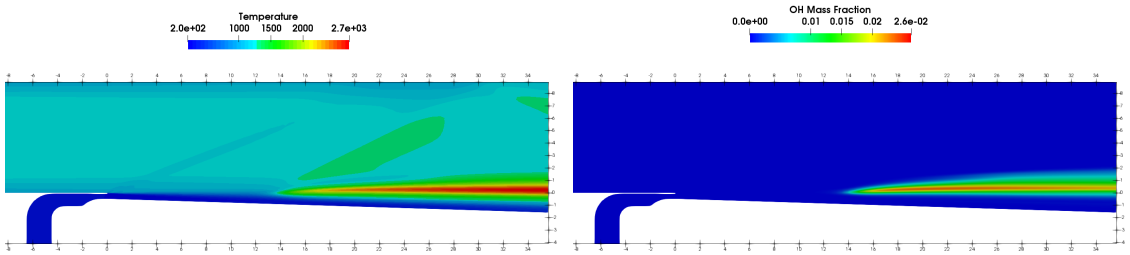

Figure 7. Contours of the temperature and $\tilde{Y}_{OH}$ obtained using UFPV at $\tilde{X}_{st} = 1.0$.

A quantitative analysis at the combustor entrance (injector step) and exit is presented in Fig. 8, where the UFPV results are compared with the FRC simulation and the experimental predictions in terms of stagnation temperature. Similar to Fig. 4, the results are in a very good agreement with the experimental data at the combustor entrance for vitiated-air mixing. This result could be improved by iterating on the facility nozzle design (true nozzle geometry was not known) that was added to allow for boundary layer development upstream of the combustor. Good agreement in terms of peak stagnation temperature is also observed at the combustor exit. Differences between FRC and UFPV can be seen in the predictions of reactive shear layer width. The FRC result shows a slightly wider width than the solution obtained from the UFPV. The location of the peak is shifted towards the lower wall of the combustor for the UFPV.

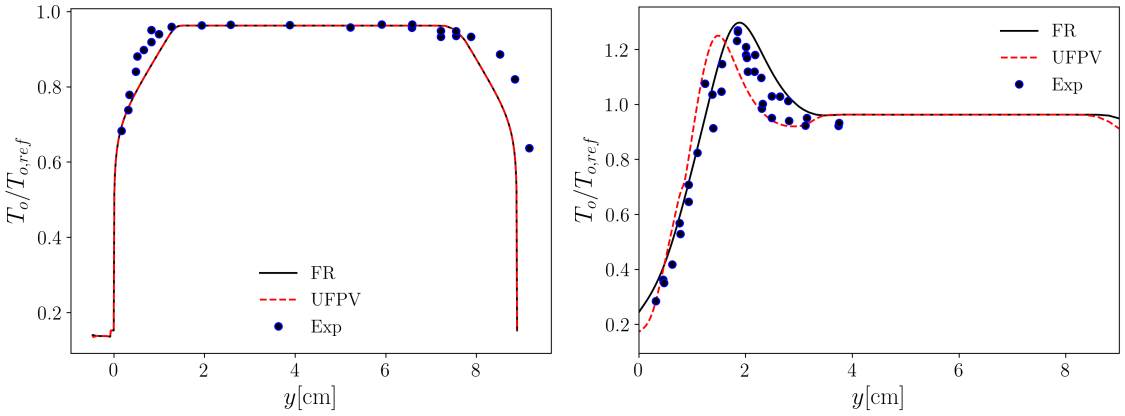

Figure 8. Stagnation temperature profiles at the step (left) and combustor exit (right) locations for the vitiated-air mixing and combustion cases, respectively.

Figure 9 presents pitot pressure profiles at the combustor inlet and exit. Similar good agreement at the entrance section is observed between the computations and the experimental data. In contrast to the stagnation temperature differences observed in the UFPV predictions, Fig. 9 indicates that UFPV yields better pitot pressure profile predictions. A shock wave forms from the flame stabilization location, and the reflection of the shock wave can be seen in Fig. 6.

Mole fraction profiles for H_2, O_2, H_2O and N_2 at the combustor exit are presented in Fig. 10. Two sets of mole fraction measurements given in[5] are included in the plots. In general, the FRC yields a better prediction than the UFPV for all mole fraction profiles. Evidence of shear layer shift in the UFPV predictions can be also seen in these plots. However, the peak value of the H_2O mole fraction obtained using UFPV is in a good agreement with the FRC.

Overall, the UFPV results are in an acceptable agreement with the FRC simulation and the experimental data.

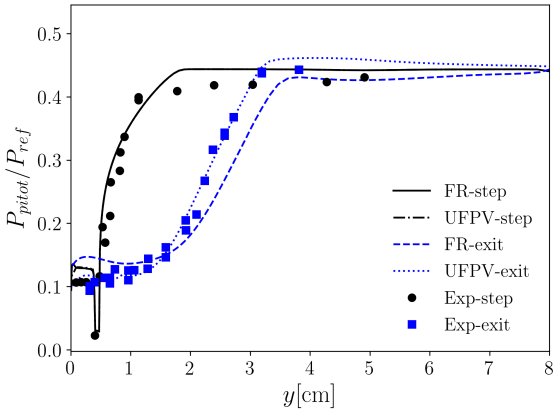

Figure 9. Pitot pressure profiles at the step and combustor exit locations for the vitiated-air mixing (black) and combustion cases (blue).

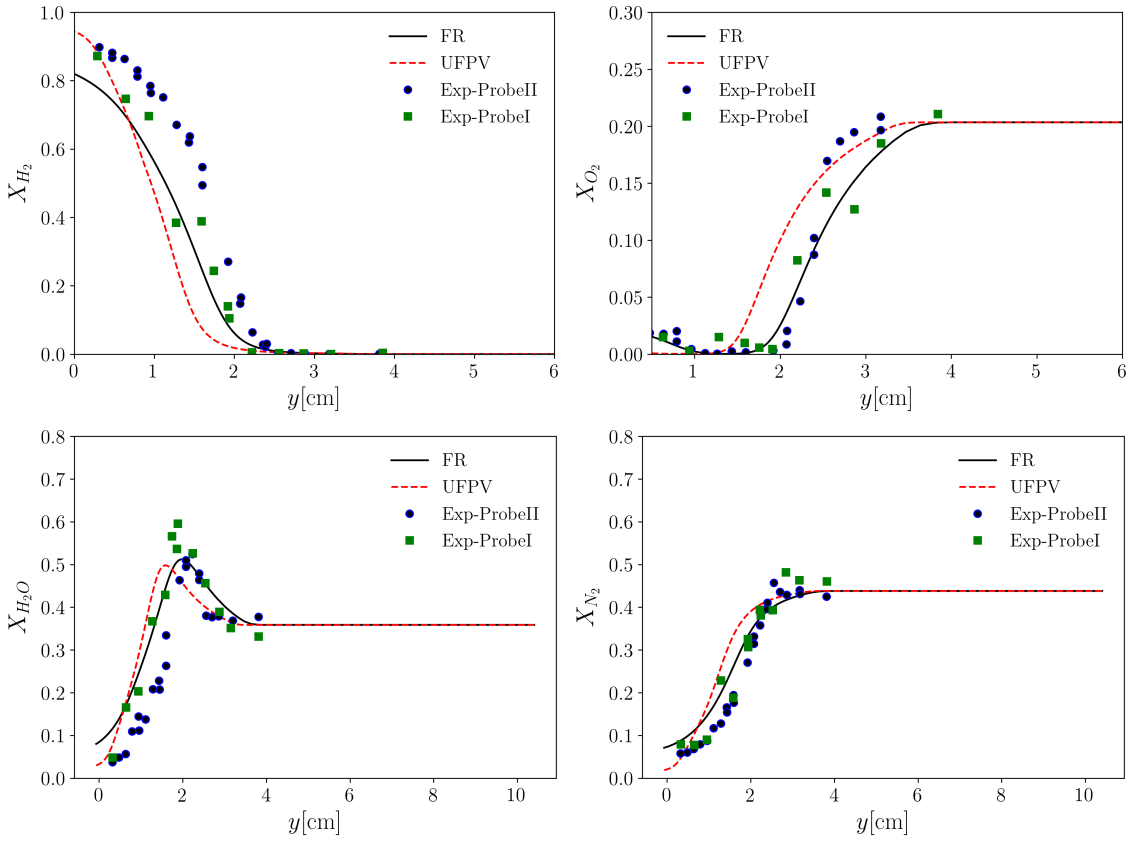

Figure 10. Mole fraction profiles at the combustor exit.

C. UFPV-ANN results

Figure 11 shows the regression plots for the mass fractions of H_2, H_2O, OH and N_2. The y-axes correspond to ANN predictions while x-axes represent target values for the ANN. One would expect excellent training once the correlation coefficients $R \rightarrow 1$ such that all the scatter data lays on the blue diagonal line. Mass fractions of the species show accurate and acceptable training results since R values are close 1.

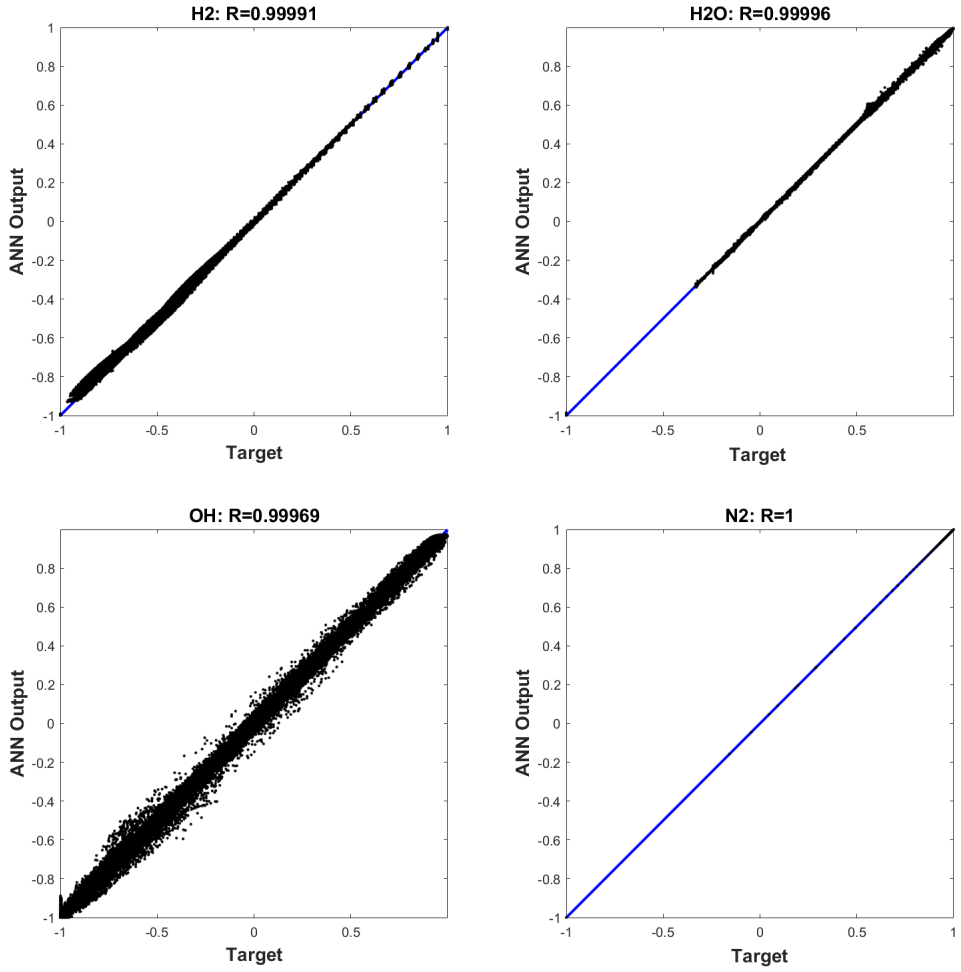

Figure 11. Regression plots comparing ANN predictions to target values for different independent variables.

The accuracy of the UFPV-ANN simulation is assessed by comparing the UFPV-ANN predictions with the base UFPV approach presented in the previous section. Snaphots of the temperature and OH mass fractions are shown in Fig. 12 for the UFPV-ANN. These results are in very good agreement with the result of UFPV shown in Fig. 6 with regard to flame stabilization, lift-off length, orientation, and flame front locations. The temperature zone of the shock wave emerging from the flame ignition point is slightly lower for the UFPV-ANN. Figure 13 confirms a very good agreement between UFPV and UFPV-ANN in terms of the stagnation temperature, pitot pressure and mole fraction profiles at the combustor exit. The peak in temperature is slightly over predicted by ANN by approximately 50K, but all of the other profiles are well captured in the ANN simulation.

As a result, the qualitative and quantitative results showed that the data-driven ANN training procedure and the UFPV-ANN framework is able to reproduce results of the base UFPV. The size of the 5-dimensional flamelet table was 396 MB whereas the size of the weights for the UFPV-ANN approach was 128 KB. The ANN approach can significantly reduce the memory footprint of the flamelet models, and at the same time retrieve the same solution as that of the multi-dimensional manifold. It should be noted that the source term in this study was retrieved via interpolation from the table. In terms of speed, the current UFPV-ANN framework runs about two times slower than UFPV. The current ANN training method utilizes a single-target ANN (ST-ANN) approach, in which each target variable is trained separately. As stated in Ref.,[15] this approach is expensive in terms of training time and computational run-time. An alternative approach, called grouped target ANN (GMT-ANN), proposed in Ref.[15] can accommodate the trade-offs between computational cost and accuracy. Briefly, the GMT-ANN aims to group similar species based on their correlation coefficients, and each group, rather than individual specie, is trained. It was shown that the GMT-ANN

approach presents reasonable simulation times and prediction accuracy for large chemical mechanisms (>20 species). We aim to examine this technique in a future study for supersonic flames so that UFPV-ANN not only provides memory optimization but also computational savings while maintaining prediction accuracy.

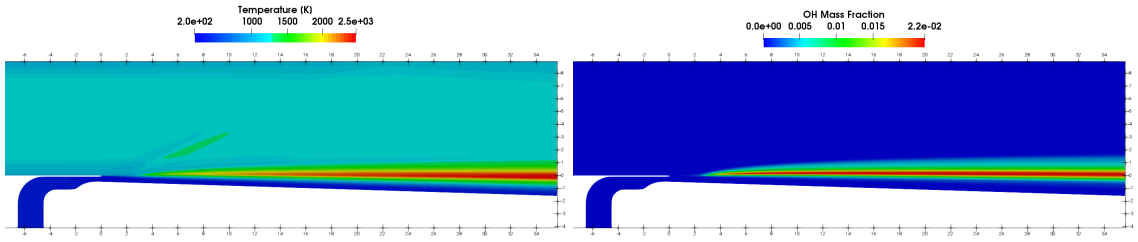

Figure 12. Contours of the temperature and $\tilde{Y}_{OH}$ obtained using UFPV-ANN.

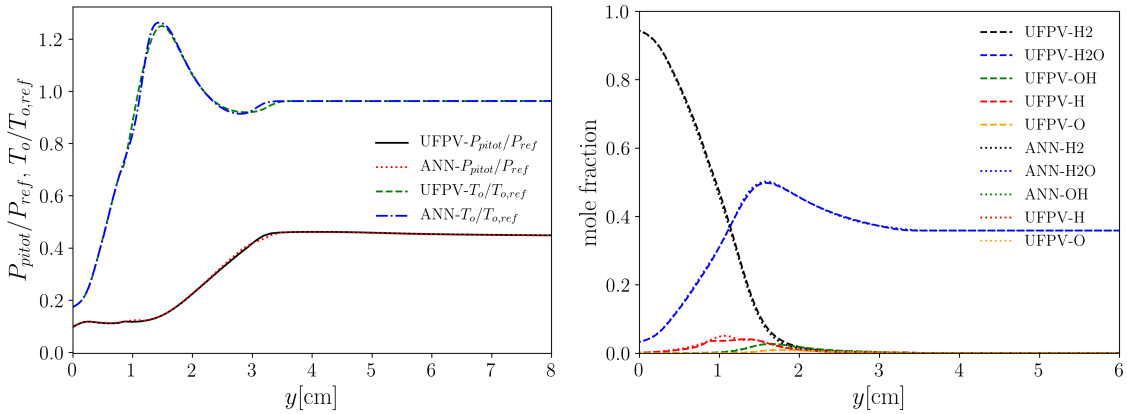

Figure 13. Pitot pressure and stagnation temperature (left), and mole fraction profiles (right) for UFPV versus UFPV-ANN comparison.

D. Comment on the progress variable normalization

The UFPV results presented in this study were obtained using a normalized progress variable approach. In this approach, the initial progress variable Y_C, which is a function of mixture fraction, is normalized as defined in Eq. 6, such that table values are bounded between 0 and 1 in both mixture fraction and progress variable space. After ensuring functional independency between Z and C in a regularization step, a remapping (interpolation) procedure is applied to obtain the species mass fractions and the source term on the newly defined normalized progress variable space. As a result, the final flamelet table contains the normalized progress variable and source term. In the CFD domain, the transport equation for the normalized progress variable, and the other required transport equations, are solved and species mass fractions and the source term of the progress variable are retrieved from the table. However, one can easily argue that if $Y_{C,min}(Z, \chi_{st}, P)$ and $Y_{C,max}(Z, \chi_{st}, P)$ vary spatially due to dependency on the mixture fraction, scalar dissipation rate, and pressure, then the transport equation for C can not be obtained by simply taking the transport equation for Y_C and dividing it by the normalization factor and then pulling this term inside the derivatives. In doing so, additional terms in Eq. (5) will appear, which are ignored in the current approach.

To overcome this problem, an alternative approach was investigated. In this approach, $Y_{C,min}(Z, \chi_{st}, P)$ and $Y_{C,max}(Z, \chi_{st}, P)$ are tabulated in the flamelet table along with the normalized progress variable, and the non-normalized progress variable transport equation was solved in the CFD domain. The transported progress variable was then normalized before the table look-up for retrieving the species mass fractions and the source term. This resulted in a significantly lower peak static temperature ($\sim$ 400K) at the combustor exit as shown in Fig. 14. It should be

noted that identical results between the normalized and non-normalized approaches are observed when the exercises above are repeated in a 0-D constant volume homogeneous reactor configuration. The main difference between the Burrows-Kurkov and the homogeneous reactor cases is that the mixture fraction remains constant during the entire calculation for the homogeneous reactor cases, therefore the progress variable normalization factor is a constant which can be moved outside the derivatives of the progress variable transport equation.

The benefit of normalization is memory storage. While the non-normalized progress variable provides the more consistent definition, it is inefficient to store in a square table with regularly space grid points. The result is a significantly lower table resolution away from the stoichiometric point, especially at extremely rich and lean conditions. Normalizing the table provides even spacing between each point and equivalent resolution across the table. Further investigations to understand the differences in the solutions depending on whether a normalized or non-normalized progress variable is solved for in the CFD domain are in progress.

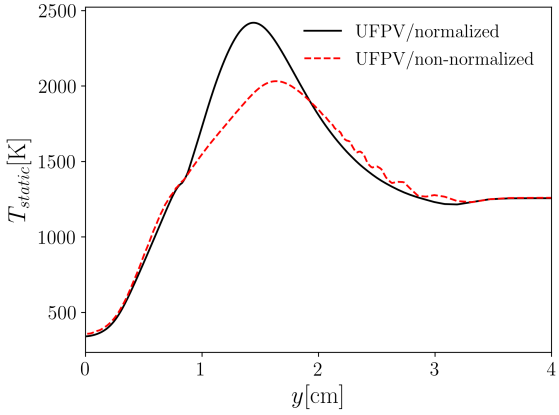

Figure 14. Comparison of two UFPV solutions at the combustor exit obtained using normalized and non-normalized progress variable transport equation.

Conclusions

An unsteady tabulated flamelet modeling framework has been implemented in the VULCAN-CFD code with the Burrows-Kurkov supersonic test configuration used for validation of this modeling approach. The current framework can accommodate up to 5D flamelet tables using interpolation as well as a deep ANN based framework in the VULCAN-CFD code. A 4D UFPV table was used to model the lifted hydrogen flame for this configuration. The presented results show overall good quantitative agreement with the FRC simulation and the experimental results. The UFPV-ANN model predictions are also compared against the base UFPV results, and excellent agreement between the two approaches is obtained. Different results in the UPFV approach based on solving either normalized or non-normalized progress variable transport equation was observed and requires further investigation.

Acknowledgments

This manuscript has been created by UChicago Argonne, LLC, Operator of Argonne National Laboratory (Argonne). Argonne, a U.S. Department of Energy Office of Science laboratory, is operated under Contract No. DE-AC02-06CH11357. The U.S. Government retains for itself, and others acting on its behalf, a paid-up nonexclusive, irrevocable worldwide license in said article to reproduce, prepare derivative works, distribute copies to the public, and perform publicly and display publicly, by or on behalf of the Government. We gratefully acknowledge the computing resources provided on Blues and Bebop, a high-performance computing cluster operated by the Laboratory Computing Resource Center at Argonne National Laboratory. In addition, authors are thankful to Opeoluwa Owoyele for useful discussions on the ANN. This work was supported by Laboratory Directed Research and Development (LDRD) funding from Argonne National Laboratory, provided by the Director, Office of Science, of the U.S. Department of Energy under Contract No. DE-AC02-06CH11357 and the Hypersonic Airbreathing Propulsion Branch of the NASA Langley

research center under Contract No. 80LARC21T0003.

References

[1] Gonzalez-Juez, E.D., Kerstein, A.R., Ranjan, R., and Menon, S., "Advances and Challenges in Modeling High-speed Turbulent Combustion in Propulsion Systems," *Progress in Energy and Combustion Science*, Vol. 60, 2017, pp. 26–67.

[2] Drozda, T.G., Quinlan, J.R., and Drummond, J.P., "Flamelet Modeling for Supersonic Combustion," Springer, Singapore, 2020, pp. 127–168.

[3] Quinlan, J.R., Drozda, T.G., McDaniel, J.C., Lacaze, G., and Oefelein, J.C., "A Priori Analysis of a Compressible Flamelet Model Using RANS Data for a Dual-Mode Scramjet Combustor," in *22nd AIAA Computational Fluid Dynamics Conference*, AIAA 2015-3208, AIAA, Dallas, TX, 2015.

[4] Demir, S., Kundu, P., and Owoyele, O., "Implementation of High Dimensional Flamelet Manifolds for Supersonic Combustion Using Deep Neural Networks," in *AIAA Aviation Forum*, AIAA 2020-3059, AIAA, Virtual Event, 2020.

[5] Burrows, M.C. and Kurkov, A.P., "Supersonic Combustion of Hydrogen in a Vitiated Air Stream Using Stepped Wall Injection," *NASA-TM-X-67840*, 1971.

[6] Burrows, M.C. and Kurkov, A.P., "Analytical and Experimental Study of Supersonic Combustion of Hydrogen in a Vitiated Airstream," *NASA-TM-X-2828*, 1973.

[7] Kundu, P., Ameen, M.M., Xu, C., Unnikrishnan, U., Lu, T., and Som, S., "Implementation of Detailed Chemistry Mechanisms in Engine Simulations," *Journal of Engineering for Gas Turbines and Power*, Vol. 141, No. 1, 2018.

[8] Edwards, J.R., Boles, J.A., and Baurle, R.A., "Large-eddy/Reynolds-averaged Navier–Stokes Simulation of a Supersonic Reacting Wall Jet," *Combustion and Flame*, Vol. 159, No. 3, 2012, pp. 1127–1138.

[9] Gao, Z., Jiang, C., and Lee, C.H., "On the Laminar Finite Rate Model and Flamelet Model for Supersonic Turbulent Combustion Flows," *International Journal of Hydrogen Energy*, Vol. 41, No. 30, 2016, pp. 13238–13253.

[10] Wu, W., Piao, Y., Xie, Q., and Ren, Z., "Flame Diagnostics with a Conservative Representation of Chemical Explosive Mode Analysis," *AIAA Journal*, Vol. 57, No. 4, 2019, pp. 1355–1363.

[11] McBride, B.J., *Computer Program for Calculation of Complex Chemical Equilibrium Compositions and Applications*, Vol. 2, NASA Lewis Research Center, 1996.

[12] Strelets, M., "Detached Eddy Simulation of Massively Separated Flows," in *39th Aerospace Sciences Meeting and Exhibit*, AIAA 2001-879, AIAA, Reno, Nevada, 2001.

[13] Bajaj, C., Ameen, M., and Abraham, J., "Evaluation of an Unsteady Flamelet Progress Variable Model for Autoignition and Flame Lift-Off in Diesel Jets," *Combustion Science and Technology*, Vol. 185, No. 3, 2013, pp. 454–472.

[14] Peters, N., "Laminar Diffusion Flamelet Models in Non-Premixed Turbulent Combustion," *Progress in Energy and Combustion Science*, Vol. 10, No. 3, 1984, pp. 319–339.

[15] Owoyele, O., Kundu, P., Ameen, M.M., Echekki, T., and Som, S., "Application of Deep Artificial Neural Networks to Multi-Dimensional Flamelet Libraries and Spray Flames," *International Journal of Engine Research*, Vol. 21, No. 1, 2020, pp. 151–168.